Available online at www.sciencedirect.com
ScienceDirect
International Journal of Heat and Fluid Flow 28 (2007) 1291–1301
International Journal of HEAT AND FLUID FLOW
www.elsevier.com/locate/ijhff

DNS of heat transfer in turbulent and transitional channel flow obstructed by rectangular prisms

Fusao Kawamura, Yohji Seki, Kaoru Iwamoto, Hiroshi Kawamura *

Department of Mechanical Engineering, Tokyo University of Science, Noda-shi, Chiba 278-8510, Japan

Received 19 December 2006; received in revised form 17 July 2007; accepted 19 July 2007
Available online 22 October 2007

Abstract

Direct numerical simulation (DNS) of heat transfer in a channel flow obstructed by rectangular prisms has been performed for $Re_\tau = 80$–20, where Re_τ is based on the friction velocity, the channel half width and the kinematic viscosity. The molecular Prandtl number is set to be 0.71. The flow remains unsteady down to $Re_\tau = 40$ owing to the disturbance induced by the prism. For $Re_\tau = 30$ and 20, the flow results in a steady laminar flow. In the vicinity of the prism, the three-dimensional complex vortices are generated and heat transfer is enhanced. The Reynolds number effect on the time-averaged vortex structure and the local Nusselt number are investigated. The mechanism of the heat transfer enhancement is discussed. In addition, the mean flow parameters such as the friction factor and the Nusselt number are examined in comparison with existing DNS and experimental data.

Keywords: Direct numerical simulation; Turbulent heat transfer; Transitional channel flow; Rectangular prism; Three-dimensional obstacle

1. Introduction

A channel flow obstructed by a bluff body can be found in various engineering fields. Owing to separation and reattachment in the vicinity of the obstacle, heat and momentum transfers are augmented. These advantages are often utilized in many practical applications such as a cooling channel in a turbine blade, a heat exchanger and an electronic device. Therefore, it is of practical importance to clarify the vortical structure and local heat transfer around the obstacle.

A channel flow with a wall-mounted prismatic obstacle has been subject to a number of previous investigations. The experimental studies of Larousse et al. (1991), Martinuzzi and Tropea (1993), Hussein and Martinuzzi (1996) focused on the flow structures around a prismatic obstacle in a fully developed channel flow for $Re_m = 10^5$–10^6, which is based on the bulk mean velocity u_m, the kinematic viscosity v and the whole channel width 2δ. The major flow structures, such as the horseshoe vortex induced around the upstream face, the arc-shaped vortex in the wake of the obstacle and the flow recirculation at the top and the side faces of the obstacle, were described. Hwang and Yang (2004) carried out numerical simulation for $Re_m = 10$–3000 to examine the Reynolds number effect on the vortex structure. They mentioned that the flow becomes turbulent in the near wake region including the free-shear layer at relatively low Reynolds numbers. Recently, Yakhot et al. (2006) performed direct numerical simulation of a channel flow with a wall-mounted cube for $Re_m = 5610$ with the use of an immersed boundary method. The time-averaged data of the turbulence mean-square intensities, Reynolds shear stresses, turbulent kinetic energy and dissipation rate are presented in their paper. As for the heat transfer of a wall-mounted cubic obstacle in a developing turbulent channel flow, Meinders et al. (1999) experimentally studied for $Re_m = 9000$–$16{,}000$. They presented the distributions of the local heat transfer on the faces of the cubic obstacle and the correlation with the flow pattern. Meinders and Hanjalić (1999), in addition, reported on the flow structure

* Corresponding author.
E-mail address: kawa@rs.noda.tus.ac.jp (H. Kawamura).

0142-727X/$ - see front matter © 2007 Elsevier Inc. All rights reserved.
doi:10.1016/j.ijheatfluidflow.2007.07.009

and the local heat transfer around a cube placed in a spatially periodic in-line matrix of cubes.

In the present study, we target a channel flow obstructed by periodically placed rectangular prisms as shown in Fig. 1. This configuration models an annular channel with spacers often seen in heat exchangers or a fuel channel of a gas cooled nuclear reactor (JAERI, 1999). Coolant flows in a narrow annular channel, in which prisms are equipped periodically in both streamwise and azimuthal directions. The prisms reach from bottom to top wall to serve as a spacer. Since the channel width is much smaller than the radius of the annulus, the channel can be modeled with the one bounded by two parallel plates. The flow is generally dependent on Reynolds number and the geometry, i.e. the size as well as the stream- and spanwise spacing of the prism. Especially in the turbulent-laminar transition range, the flow and the thermal fields are more dramatically affected by the obstacle than in high Reynolds numbers because separation and reattachment around the obstacle promote turbulence. Hence, in the present work, a series of DNS has been performed at low Reynolds numbers of $Re_\tau = u_{\tau 0}\delta/v = 80$–$20$, where $u_{\tau 0}$ is the friction velocity defined by the pressure gradient to drive the flow.

The objective of this work is to explore the local effects of the turbulence enhancement by obstacles on the velocity and temperature fields. The effect of the Reynolds number is studied in the turbulent-laminar transition range for an assumed geometry, which is determined in reference to a spacer rib in the coolant channel of the gas cooled nuclear reactor (JAERI, 1999). As for the geometrical effect, the spacing of the prism has been examined; however, it turned out that the spacing of this design is rather large so that it causes no large primary effect on the fundamental characteristics of the velocity and temperature fields. Aspect ratio of the prism may cause larger effects, but the large computational burden enabled us to perform one series of computation for the given design of the fuel channel. The relation between the vortices generated in the vicinity of the obstacle and local heat transfer is discussed. In addition, the mean flow parameter such as the friction factor and the Nusselt number are discussed in comparison with existing DNS and experimental data.

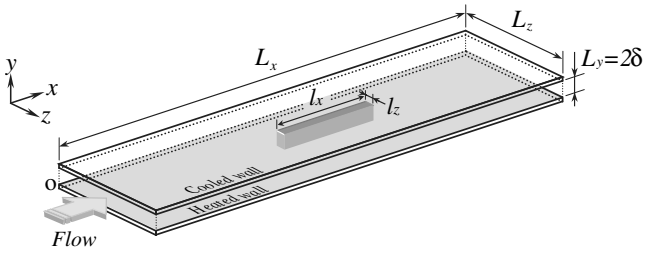

Fig. 1. Configuration of the computational domain.

2. Numerical procedures

Fig. 1 shows the configuration of the computational domain. The rectangular prism is located at the center of the domain and directly connected to both the top and the bottom walls. In the x- and z-directions, the periodic boundary condition is applied, i.e. the prism is periodically located in the streamwise and the spanwise directions. The flow is assumed an incompressible viscous fluid with a passive temperature field. It is driven by the streamwise mean pressure gradient. The continuity, the Navier–Stokes and the energy equations are solved. All the variables are normalized by the friction velocity $u_{\tau 0}(=[-(\delta/\rho)(\mathrm{d}\overline{p}/\mathrm{d}x)]^{1/2})$, the channel half width δ and the temperature difference $\Delta T(=T_{\mathrm{bottom}} - T_{\mathrm{top}})$. Here, ρ is the density and $\mathrm{d}\overline{p}/\mathrm{d}x$ the mean pressure gradient imposed to maintain the flow. The temperature difference between the top and the bottom walls is kept constant.

In the present computation, the fractional step method proposed by Dukowicz and Dvinsky (1992) is adopted, and a semi-implicit time advancement is used. For the viscous terms with wall-normal derivatives, the Crank–Nicolson method is employed. For the other terms, the second-order Adams–Bashforth method is applied. For the spatial discretization, the finite difference method is used. The numerical scheme proposed by Morinishi et al. (1998) with the fourth-order accuracy is adopted in the streamwise and spanwise directions, whereas the second-order one in the wall-normal direction.

The non-slip condition is imposed on the top and the bottom walls, whilst the prism is computed with the use of the immersed boundary method described in detail by Fadlun et al. (2000). It consists of imposing the desired velocity value (i.e. zero in this case) on the body surface by an adequate treatment of the external force term in the Navier–Stokes equation. As regards the temperature on the surface of the prism, a linear profile ($T = 1 - y^*/2$)

Table 1
Computational conditions

$Re_\tau(=u_{\tau 0}\cdot\delta/v)$	20	30	40	50	60	80
$Re_{\mathrm{m}}(=u_{\mathrm{m}}\cdot 2\delta/v)$	240	510	770	1000	1240	1780
$Pr(=v/\kappa)$				0.71		
$L_x\times L_y\times L_z$				$51.2\delta\times 2\delta\times 12.8\delta$		
$l_x\times l_z$				$11.4\delta\times 1.3\delta$		
$N_x\times N_y\times N_z$				$1024\times 128\times 256$		
$\Delta x^*, \Delta y^*_{\mathrm{min}} - \Delta y^*_{\mathrm{max}}, \Delta z^*$				0.05,0.0001–0.033,0.05		
$\mathcal{T}u_{\mathrm{m}}/L_x(\mathcal{T}u_{\tau 0}/\delta)$	–	–	52 (280)	54 (280)	89 (440)	78 (360)

Table 2
Comparison of mesh resolutions with Kolmogorov's length scale

Re_τ	$\gamma(=(\Delta x\Delta y\Delta z)^{-1/3}/\eta)$	$\gamma_x(=\Delta x/\eta)$	$\gamma_y(=\Delta y/\eta)$	$\gamma_z(=\Delta z/\eta)$
80	$0.22 \leqslant \gamma \leqslant 3.69$	$0.47 \leqslant \gamma_x \leqslant 5.95$	$0.03 \leqslant \gamma_y \leqslant 2.79$	$0.47 \leqslant \gamma_z \leqslant 5.95$
60	$0.17 \leqslant \gamma \leqslant 2.72$	$0.35 \leqslant \gamma_x \leqslant 4.45$	$0.02 \leqslant \gamma_y \leqslant 1.99$	$0.35 \leqslant \gamma_z \leqslant 4.45$
40	$0.10 \leqslant \gamma \leqslant 1.73$	$0.17 \leqslant \gamma_x \leqslant 2.68$	$0.02 \leqslant \gamma_y \leqslant 1.31$	$0.17 \leqslant \gamma_z \leqslant 2.68$

is imposed with the assumption that the heat conductivity of the prism is much larger than that of the fluid.

The computational domain size ($L_x \times L_y \times L_z$), the prism size ($l_x \times l_z$), the number of grid points ($N_x \times N_y \times N_z$), the spatial resolution ($\Delta x, \Delta y, \Delta z$) and the sampling time period for time-average ($\mathscr{T} u_m/L_x$) are given in Table 1, where u_m, κ and $\mathscr{T}$ are the resultant bulk mean velocity, the thermal diffusivity and the sampling time, respectively. The accuracy of the DNS depends upon the mesh resolution. The relationship between the mesh resolution and the Kolmogorov's length scale η are summarized in Table 2 in the cases of $Re_\tau = 80$, 60 and 40. From the authors' experience reported by Seki et al. (2006), these resolutions are enough small to obtain the second-order statistics of turbulence.

3. Results and discussion

3.1. Instantaneous flow field

Fig. 2 shows the isosurfaces of the low-speed velocity fluctuations u' and of the negative second invariant of deformation tensor $II(=\partial u_i/\partial x_j \times \partial u_j/\partial x_i)$ in an instantaneous flow field for $Re_\tau = 80$–30, respectively. It is well known that the negative region of the second invariant well represents the vortex region (see e.g. Robinson (1991)).

For $Re_\tau = 80$, the near-wall streaky structures and the vortices are distributed in the whole calculated domain as seen in Fig. 2a. In particular, a lot of complex vortices are observed in the side and the downstream regions of the prism. Note that the unsteady horseshoe vortices are generated in the vicinity of the upstream face of the prism. In case of the plane channel flow, Tsukahara et al. (2005) reported the periodic intermittent flow alternated by a quasi-laminar and a highly disordered turbulent states at $Re_\tau = 80$ ($Re_m = 2320$). If we look at our results at the same mean pressure drop, i.e. $Re_\tau = 80$ and $Re_m = 1780$, the flow is still turbulent and no such the intermittency is observed, although, in case of the plane channel flow at the same mean Reynolds number ($Re_m = 1780$), the flow is already laminar.

With decreasing Re_τ, the near-wall streaky structures are still distributed in the whole domain for $Re_\tau = 60$ and 50 (see Fig. 2b and c). Except in the wake region, however, the areas of weak-turbulence with few vortices are observed. With further reduction of Re_τ down to 40, the number of near-wall streaky structures significantly decreases especially outside the wake region. Note that the steady laminar flow is observed at $Re_\tau = 30$ as shown in Fig. 2e and $Re_\tau = 20$ (not shown here).

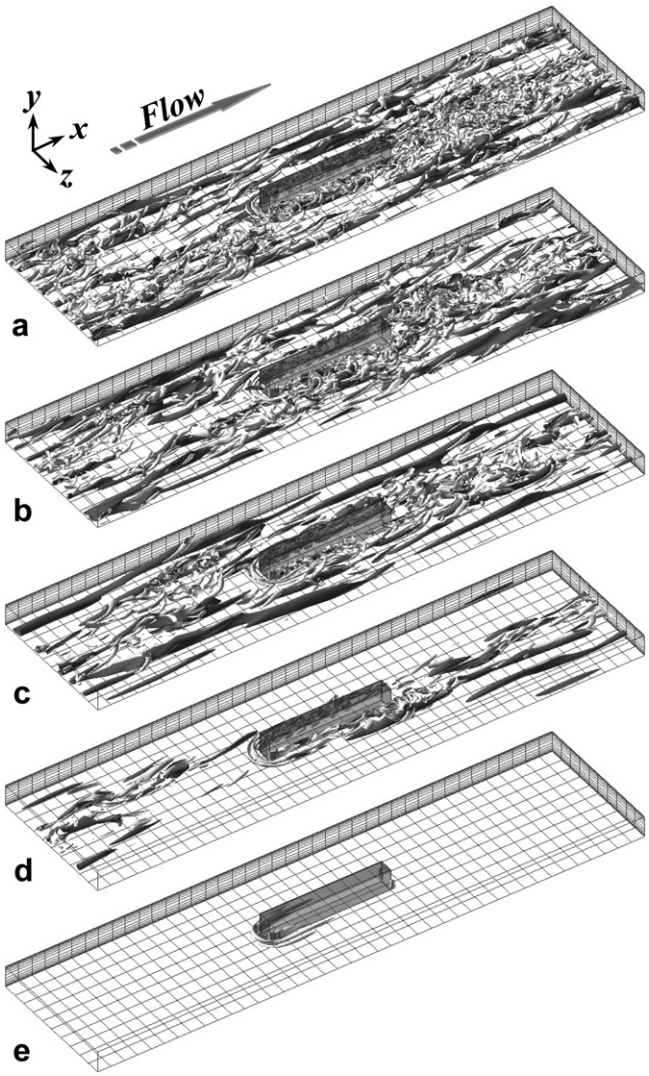

Fig. 2. Instantaneous flow fields; (a) $Re_\tau = 80$; (b) $Re_\tau = 60$; (c) $Re_\tau = 50$; (d) $Re_\tau = 40$; (e) $Re_\tau = 30$. The low-speed regions of u' and the negative regions of the second invariant of deformation tensor II (dark gray, $u'^+ \leqslant -2.0$; light gray, $II^+ \leqslant -0.01$). Here, the superscript of + denotes normalization by v and $u_{\tau 0}$. Lower half domain is visualized.

3.2. Vortex structure and local heat transfer in time-averaged flow field

The upstream flow is not fully recovered for all the calculated cases although a series of DNS has been carried out

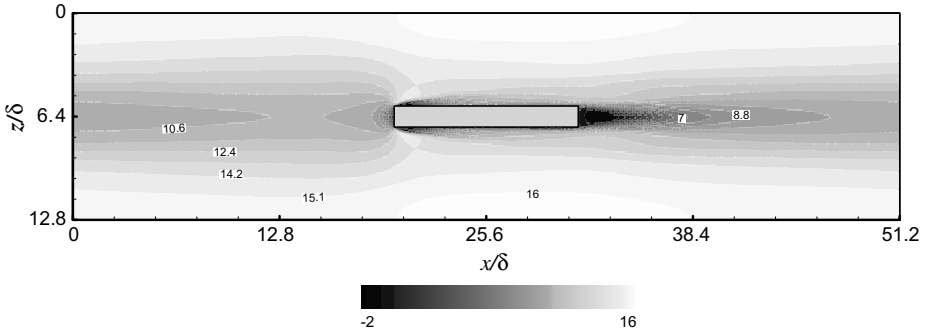

Fig. 3. Contours of the time-averaged velocity $\overline{u}^+$ in the x–z plane at the channel central height for $Re_\tau = 60$.

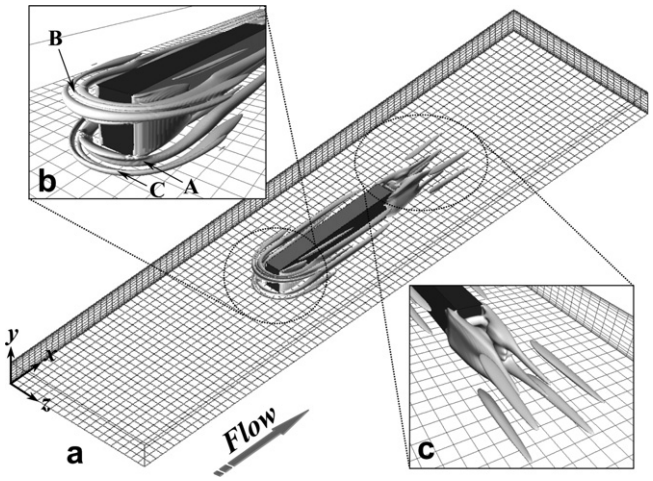

Fig. 4. Vortex structure in the time-averaged flow field at $Re_\tau = 60$; the negative regions of the second invariant of deformation tensor $\overline{II}$ (isosurfaces, $\overline{II}^+ \leqslant -1.0 \times 10^{-3}$).

with using relatively large computational domain. Fig. 3 shows the contours of the time-averaged velocity $\overline{u}^+$ in the x–z plane at the channel center for $Re_\tau = 60$ for instance. The wake reaches to the upstream of the prism. The strong wake, however, decays in between. In the vicinity of the prism, the three-dimensional vortices are generated similarly to the cases of the cited works in Section 1. A birds-eye view of the time-averaged vortex structures at $Re_\tau = 60$, for example, is shown in Fig. 4. The complex vortices wrap around the prism. Upstream of the prism, a cluster of the horseshoe vortices is separately formed at the top and the bottom prism bases. The individual cluster consists of three vortices (A, B and C) as seen in Fig. 4b. These vortices are elongated streamwise along the side faces of the prism. Downstream of the prism, four longitudinal vortices are observed near the wake region (see Fig. 4c). Note that this combination of vortex structures is unchanged for all the calculated cases.

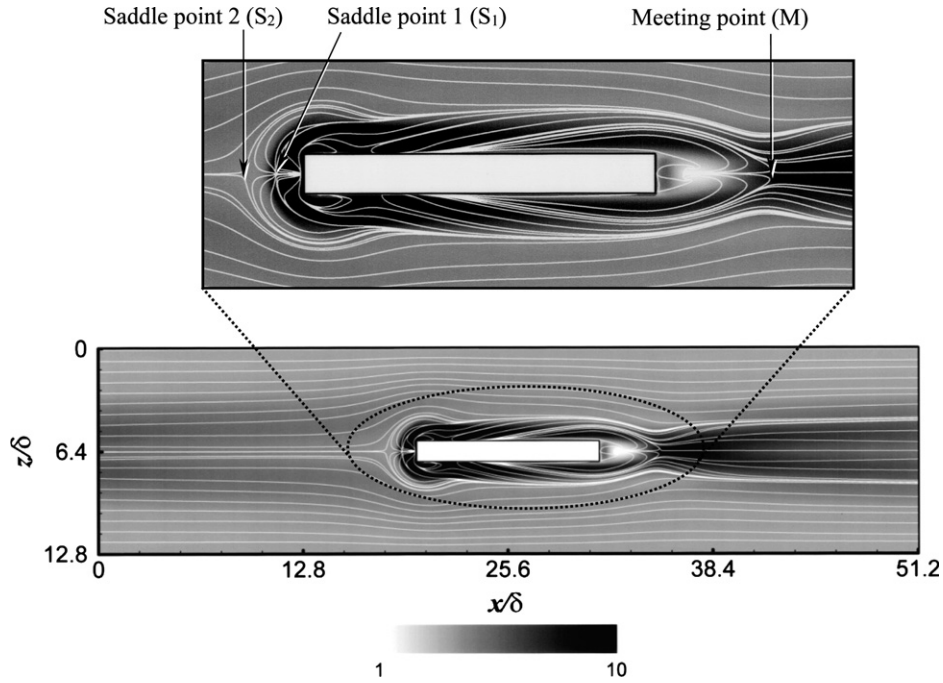

Fig. 5. Contours of the local Nusselt number $\overline{Nu}$ on the bottom wall at $Re_\tau = 60$. The lines represent the limited streamlines of the mean flow in the x–z plane at $y/\delta = 0.05$.

Fig. 5 shows the contours of the time-averaged local Nusselt number $\overline{Nu}$ on the wall at $Re_\tau = 60$, for example. Here, the time-averaged local Nusselt number $\overline{Nu}$ is defined as

$$\overline{Nu} = \left| \frac{\overline{q_w} \cdot 2\delta}{(\overline{T_m} - T_w)\lambda} \right|, \quad (1)$$

where $\overline{q_w}$ is the time-averaged local heat flux at the wall, $\overline{T_m}$ the time-averaged bulk mean temperature, T_w the temperature at the wall and λ the thermal conductivity of the fluid. Hereafter, the overbar denotes an average over time. In Fig. 5, the lines represent the streamlines drawn by two-dimensional time-averaged velocity vectors in the x–z plane at $y/\delta = 0.05$. The flow pattern is very similar to that of a wall-mounted prismatic obstacle reported by earlier literatures (e.g. Larousse et al., 1991; Martinuzzi and Tropea, 1993; Meinders et al., 1999). The points of S_1 and S_2 in Fig. 5 are often called saddle points. The separation lines originate at these points S_1 and S_2. Within the inner separation line, the Nusselt number $\overline{Nu}$ is remarkably increased. Downstream of the prism, the divided mean flows converge at a meeting point M. The Nusselt number $\overline{Nu}$ is also augmented around the downstream area of the meeting point M.

3.2.1. Horseshoe vortex and local heat transfer

Fig. 6 represents the time-averaged streamlines in the x–y plane of symmetry in front of the prism. In Fig. 6a, the vortices A–C correspond to those of in Fig. 4b, respectively. Although the vortex C is not clearly observed, its existence is confirmed by the negative local minimum value of $\overline{\Pi}$ as seen in Fig. 4b. The primary vortex A and the secondary vortex C are rotating in the clockwise direction, while the vortex B in the counterclockwise direction. For $Re_\tau = 80$–30, the secondary vortex C and vortex B are formed. On the other hand, they do not appear for $Re_\tau = 20$ as shown in Fig. 6d. With decreasing Reynolds number, the center of the primary horseshoe vortex (vortex A) gradually shifts towards the channel center and downstream.

Fig. 7 shows contours of the time-averaged temperature in the same plane as Fig. 6. Around the front face of the prism, i.e. the sweep side of the horseshoe vortex, the area of $T^* \approx 0.5$ extends near to the bottom walls. In particular, the temperature gradient is quite large near the bottom wall for $Re_\tau = 80$.

Fig. 8 shows the $\overline{Nu}$ and the skin friction coefficient $\overline{C_f} = \overline{\tau_w}/(\rho u_m^2/2)$ in the symmetry plane on the bottom wall. Here, τ_w is the wall shear stress. The region of negative $\overline{C_f}$ corresponds to the position where the horseshoe vortices are formed. The profiles of $\overline{C_f}$ indicate that the streamwise sizes of the horseshoe vortices are almost unchanged in the present range of Reynolds numbers except for $Re_\tau = 20$. For $Re_\tau = 80$–30, the position of the saddle point is about δ from the front-end prism for S_1 and 1.8δ for S_2. The profiles of $\overline{Nu}$ exhibit the significant

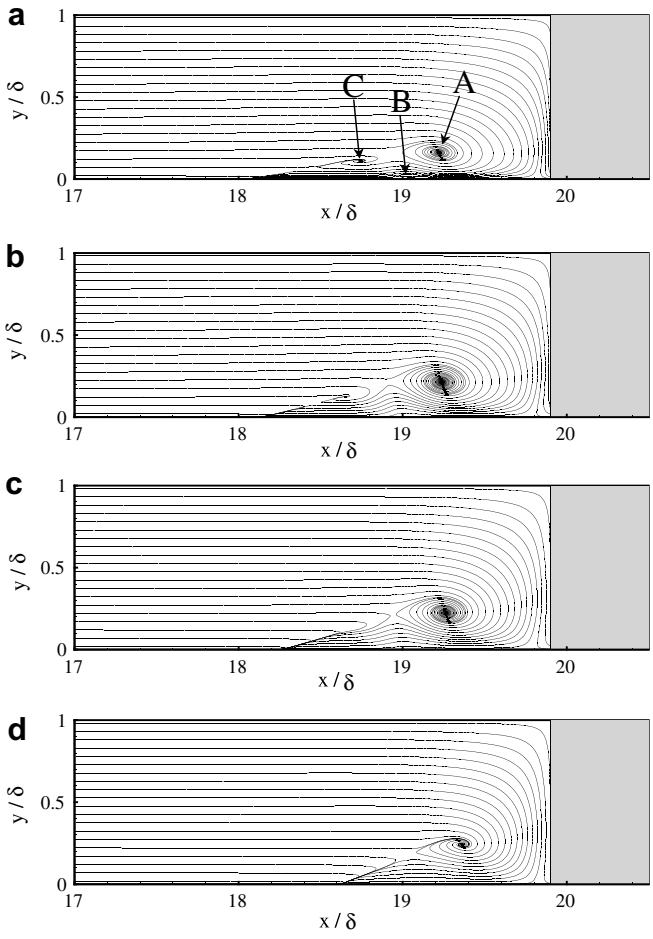

Fig. 6. Time-averaged streamlines in the upstream region of the prism in the x–y plane of symmetry ($z/\delta = 6.4$); (a) $Re_\tau = 80$; (b) $Re_\tau = 40$; (c) $Re_\tau = 30$; (d) $Re_\tau = 20$.

enhancement of the heat transfer in front of the prism. In this region, the low temperature-fluid in the mid height is transported towards the bottom wall owing to the flow impinging on the front face of the prism. In addition, the horseshoe vortices continuously remove the fluid heated by the bottom wall. Thus, the temperature gradient at the bottom wall is augmented. The individual profiles of $\overline{Nu}$ are very similar although their magnitude depends on the Reynolds number. The width of the area where $\overline{Nu}$ is remarkably enhanced is roughly δ from the front face of the prism. In addition, Fig. 8 clearly indicates that the region where $\overline{Nu}$ is high coincides well with the region where the horseshoe vortex exists. So, the close relation between the horseshoe vortices and $\overline{Nu}$ is thus confirmed.

3.2.2. Lateral vortex and local heat transfer

Fig. 9 shows the mean velocity vector components of $\overline{v}$ and $\overline{w}$ on the y–z plane at the streamwise bisection of the prism ($x/\delta = 25.6$). Four longitudinal vortices are swirling near the side face of the prism. For $Re_\tau = 80$–50, the center of these vortices are approximately unchanged. This position is 0.5δ from the wall and δ from the side face of the

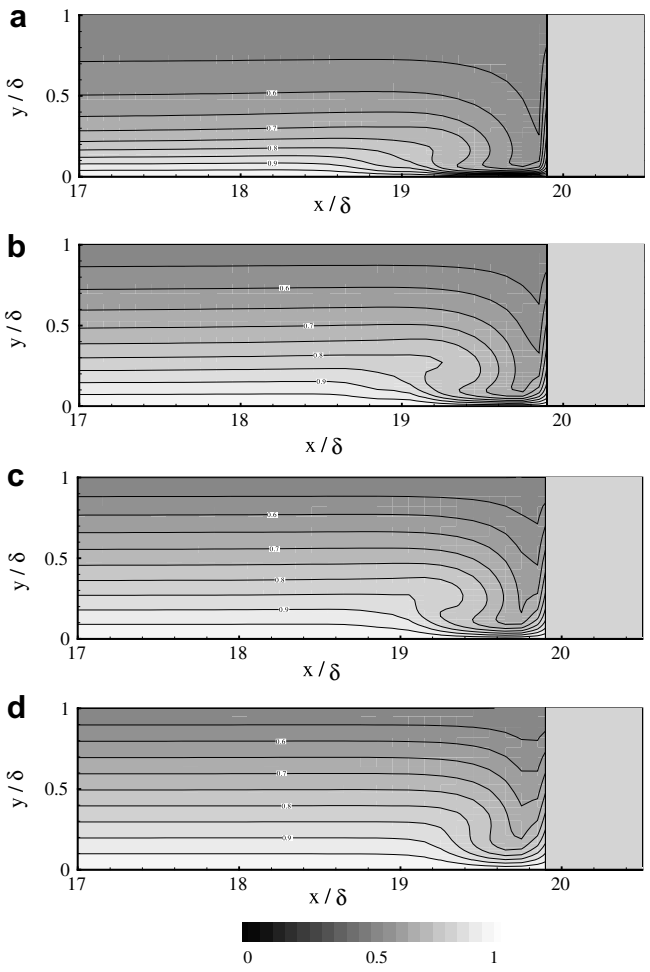

Fig. 7. Contours of the time-averaged temperature in the upstream region of the prism in the x–y plane of symmetry ($z/\delta = 6.4$); (a) $Re_\tau = 80$; (b) $Re_\tau = 40$; (c) $Re_\tau = 30$; (d) $Re_\tau = 20$.

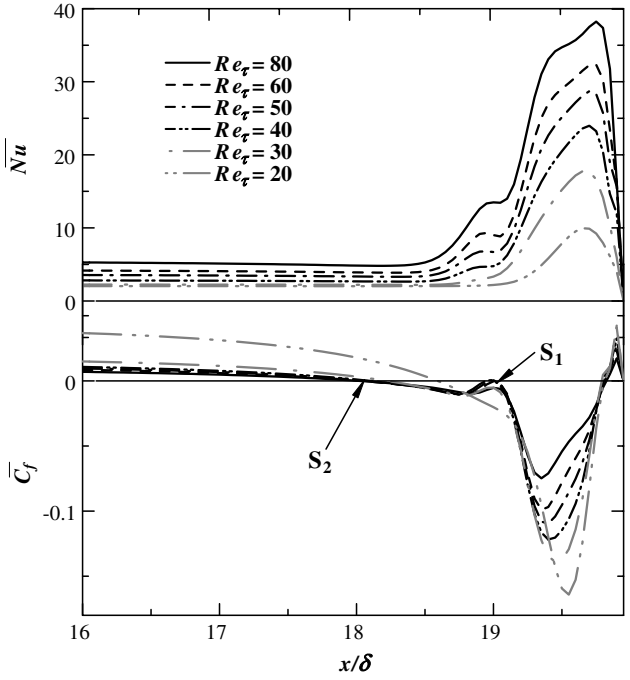

Fig. 8. $\overline{C_f}$ and $\overline{Nu}$ in front of the prism in the symmetry plane on the bottom wall.

prism. With further reduction of Reynolds number, these vortices become weak (Fig. 9b and c). Here, the center of the vortices tends to approach the side face of the prism. At the lowest Re_τ of 20, these vortices are not observed (see Fig. 9d).

The distribution of the time-averaged temperature in the same plane as Fig. 9 is presented in Fig. 10. As with the upstream region of the prism, the temperature gradient near the bottom wall is more enhanced around the sweep side of the longitudinal vortices.

Fig. 11 shows the spanwise distribution of $\overline{Nu}$ on the bottom wall at the bisection ($x/\delta = 25.6$). For $Re_\tau = 80 - 30, \overline{Nu}$ is significantly enhanced in the location where the longitudinal vortices are formed. This heat transfer enhancement is attributed to the same mechanism as that in the upstream region. The individual profiles of $\overline{Nu}$ is similar except for $Re_\tau = 20$.

3.2.3. Local heat transfer in wake region

Fig. 12 represents the time-averaged streamlines in the x–y plane of symmetry in the downstream region of the prism. The flow pattern in the downstream region strongly depends on Reynolds number in contrast to those of the horseshoe vortices and the lateral vortices. For $Re_\tau = 80$–40, the meeting line first shifts towards the downstream direction with decreasing Reynolds number. Then it approaches to the back-end prism for $Re_\tau = 30$ and 20. Moreover, the shape of the meeting line also depends on Reynolds number. Note that the two vortices are formed near the back-end of the prism inside the cavity zone for $Re_\tau = 80$–40, while they are not formed for $Re_\tau = 30$–20. The cases with or without the vortices roughly correspond to the unsteady or the steady cases, respectively.

Fig. 13 shows contours of the time-averaged temperature in the same plane as Fig. 12. Near the back-end of the prism, the fluid with a middle temperature at the mid height is transported towards the bottom wall by the vortices in the cavity zone. On the other hand, the temperature gradient become large at the channel central height in the cavity zone ($x/\delta = 32$–33).

Fig. 14 shows $\overline{C_f}$ and $\overline{Nu}$ in the downstream region of the prism in the symmetry plane on the bottom wall. The point of $\overline{C_f} = 0$ corresponds to the meeting point M shown in Fig. 5. The profiles of $\overline{Nu}$ exhibits the two the local peaks. One is at the position of the vortex in the cavity zone near the back-end prism, which is caused by the same mechanism as the upstream region. The other is at the downstream of the meeting points for $Re_\tau = 80 - 40$. This local peak arises from the enhanced mean temperature gradient owing to the effective mixing by a number of vortices behind the prism seen in Fig. 2. It has been confirmed that the turbulent heat flux $\overline{v'T'}$ is augmented in this region (not

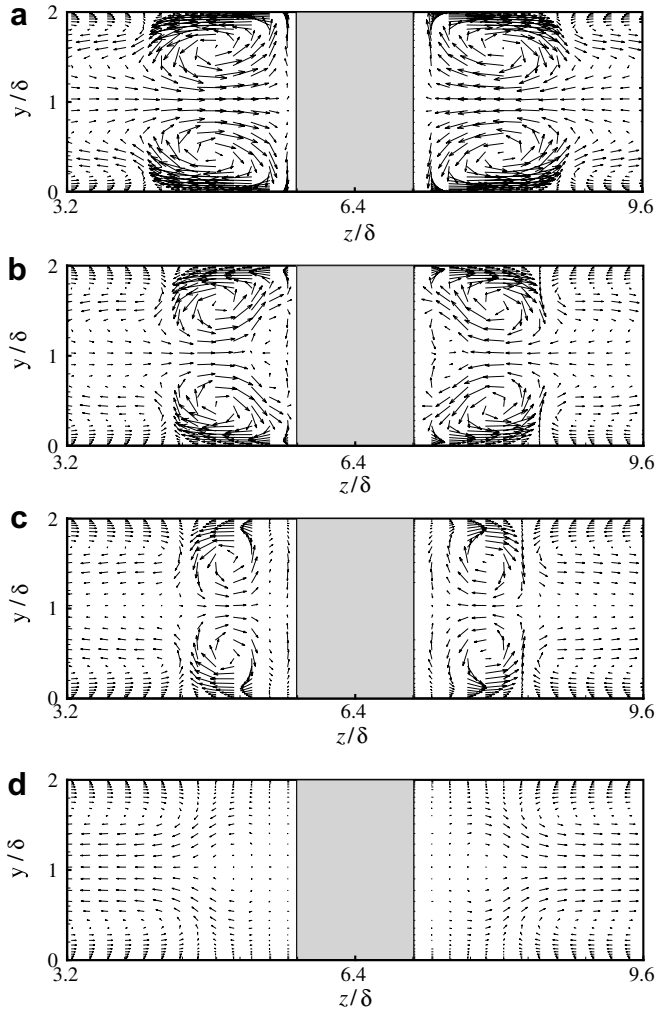

Fig. 9. Mean velocity vector components of $\overline{v}$ and $\overline{w}$ in y–z plane at $x/\delta = 25.6$; (a) $Re_\tau = 80$; (b) $Re_\tau = 40$; (c) $Re_\tau = 30$; (d) $Re_\tau = 20$.

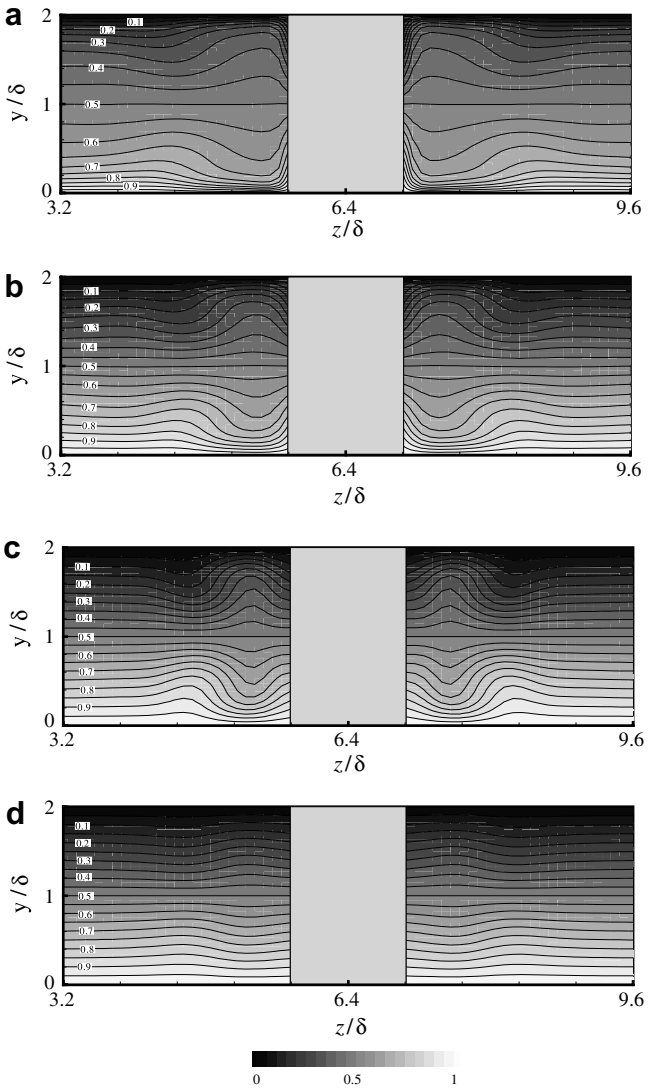

Fig. 10. Contours of the time-averaged temperature in y–z plane at $x/\delta = 25.6$; (a) $Re_\tau = 80$; (b) $Re_\tau = 40$; (c) $Re_\tau = 30$; (d) $Re_\tau = 20$.

shown here). Note that no significant correlation can be found between the meeting points and the local peaks for the calculated cases.

3.3. Mean flow parameter

Fig. 15 shows the friction factor f_A in comparison with the empirical correlations proposed by Dean (1978) for the plane channel flow and by Blasius for the pipe flow. The present friction factor is defined as follows,

$$f_A = \frac{\overline{\Delta p}}{L_x}\frac{\delta}{\rho u_m^2/2}, \tag{2}$$

where $\overline{\Delta p}$ is the time-averaged pressure drop from $x = 0$ to $x = L_x$. The friction factor f_A contains the form drag of the prism. In the transition range of plane channel flows, it is well known that f_A once decreases with decreasing Re_m. It results from that the flow becomes laminar and turbulent intermittently (see, e.g. Patel and Head, 1969; Iida and Nagano, 1998; Tsukahara et al., 2005). In the present case, however, the drop of f_A does not appear in this range. This is because the flow remains turbulent as a consequence of the disturbance induced by the prism. The similar tendency is also observed in the experimental data of an annular channel flow with spacers (JAERI, 1999).

Fig. 16 shows the time- and spatial-averaged Nusselt number $\langle\overline{Nu}\rangle$. Hereafter, the angle brackets $\langle\rangle$ denotes a spatial-average over x- and z-directions. The result of DNS for a plane channel flow with the constant temperature difference condition (Seki et al., 2003; Tsukahara et al., 2006) is also shown. In the case of the plane channel flow, Nusselt number tends to drop rapidly towards the theoretical solution of the laminar flow with decreasing the Reynolds number. On the other hand, the present $\langle\overline{Nu}\rangle$ with the prisms is higher than the empirical correlation for the turbulent channel flow. Moreover, it stays larger than the empirical correlation even in the transition range.

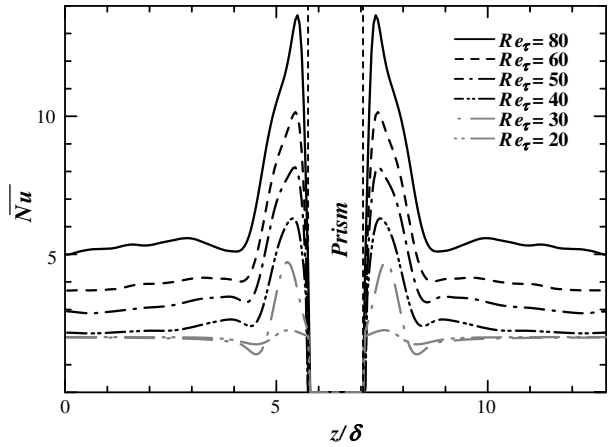

Fig. 11. $\overline{Nu}$ in y–z plane at $x/\delta = 25.6$ on the bottom wall.

To examine the contribution of the mean flow and the fluctuation to $\langle\overline{Nu}\rangle$, a mathematical relation is derived with reference to Fukagata et al. (2005). The energy equation for $\overline{T^*}$ can be written as

$$0 = -\frac{\partial}{\partial x_j^*}\overline{u_j^*}\,\overline{T^*} - \frac{\partial}{\partial x_j^*}\overline{u_j'^* T'^*} + \frac{1}{Re_m Pr}\frac{\partial^2 \overline{T^*}}{\partial x_j^{*2}}, \tag{3}$$

where u_i^* is nondimensionalized by twice the bulk mean velocity $2u_m$. The boundary conditions are $T^*|_{y^*=0} = 1, T^*|_{y^*=2} = 0$. Here, the time-averaged Nusselt number is

$$\overline{Nu} = \left|\frac{\overline{q_w}\cdot 2\delta}{(\overline{T_m} - T_w)\lambda}\right| = -\frac{2\delta}{\Delta T/2}\left.\frac{d\overline{T}}{dy}\right|_{y^*=0} = -4\left.\frac{d\overline{T^*}}{dy^*}\right|_{y^*=0}. \tag{4}$$

By integrating Eq. (3) once from 0 to y^*, we obtain

$$\frac{\overline{Nu}}{4Re_m Pr} = \overline{v^*}\,\overline{T^*} + \overline{v'^* T'^*} - \frac{1}{Re_m Pr}\frac{\partial \overline{T^*}}{\partial y^*} + \int_0^{y^*} I_{xz}\,dy^*, \tag{5}$$

where I_{xz} contains the convection and the diffusion terms in the x- and z-directions. The conditions of $\overline{v^*}\,\overline{T^*}|_{y^*=0} = 0, \overline{v'^* T'^*}|_{y^*=0} = 0$ and Eq. (4) are used to obtain Eq. (5). This integration is equivalent to obtain the flux balance. Eq. (5) is integrated again from 0 to 1 to read

$$\overline{Nu} = 2 + 4Re_m Pr\left[\int_0^1 \overline{v^*}\,\overline{T^*}\,dy^* + \int_0^1 \overline{v'^* T'^*}\,dy^* + \int_0^1\int_0^{y^*} I_{xz}\,dy^*\,dy^*\right]. \tag{6}$$

Here, the boundary condition, i.e. $\overline{T^*}|_{y^*=0} = 1$ and the anti-symmetry condition, i.e. $\overline{T^*}|_{y^*=1} = 0.5$ are used. Because of the periodicity in the stream- and spanwise directions, the integration of Eq. (6) in the x- and z-direction gives the time- and spatial-averaged Nusselt number $\langle\overline{Nu}\rangle$ as follows:

$$\langle\overline{Nu}\rangle = 2 + 4Re_m Pr\left[\left\langle\int_0^1 \overline{v^*}\,\overline{T^*}\,dy^*\right\rangle + \left\langle\int_0^1 \overline{v'^* T'^*}\,dy^*\right\rangle\right]. \tag{7}$$

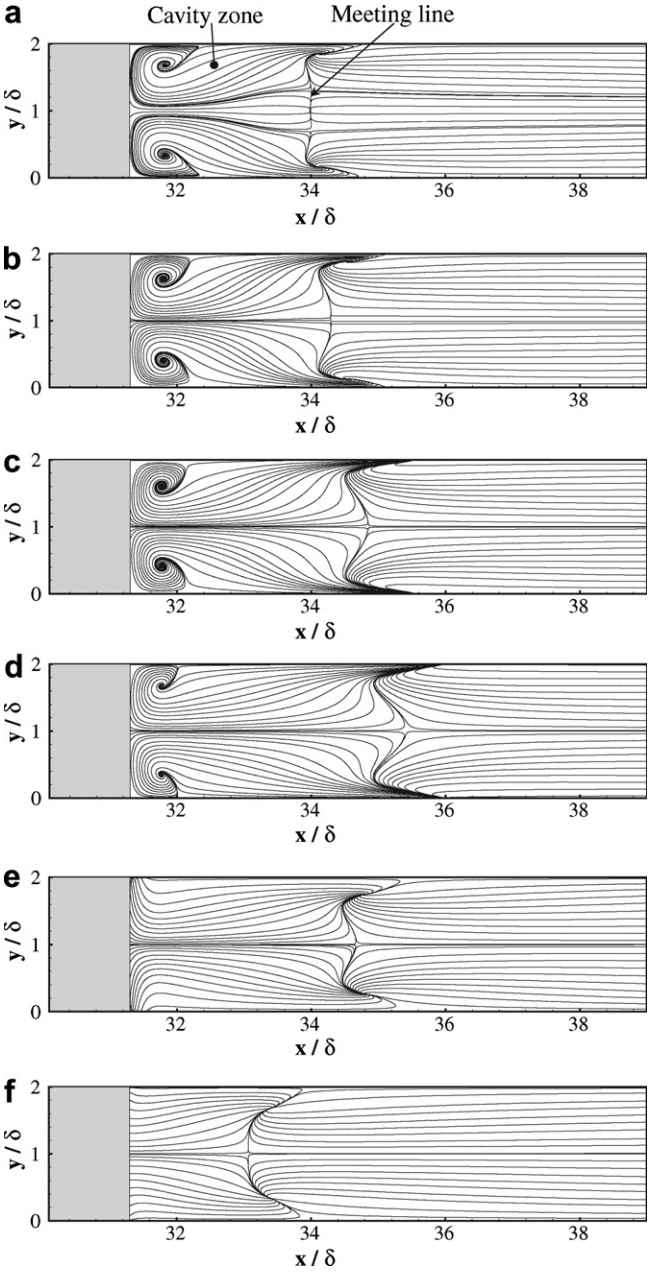

Fig. 12. Time-averaged streamlines in the downstream region of the prism in the x–y plane of symmetry; (a) $Re_\tau = 80$; (b) $Re_\tau = 60$; (c) $Re_\tau = 50$; (d) $Re_\tau = 40$; (e) $Re_\tau = 30$; (f) $Re_\tau = 20$.

Here, the heat flux from the surfaces of the prism was neglected because the volume of the prism is much smaller than the whole computational domain. The first term in the right hand side indicates the contribution of the conduction, the second term that of the convection by the mean flow and the third term that of the turbulence transport.

Each term of Eq. (7) is shown in Fig. 17. It has been confirmed that the value of $\langle\overline{Nu}\rangle$ calculated from Eq. (7) agree well with the directly calculated value shown in Fig. 16 with an accuracy of 0.5%. A notable point is that the contribution of the mean flow convection to $\langle\overline{Nu}\rangle$ is

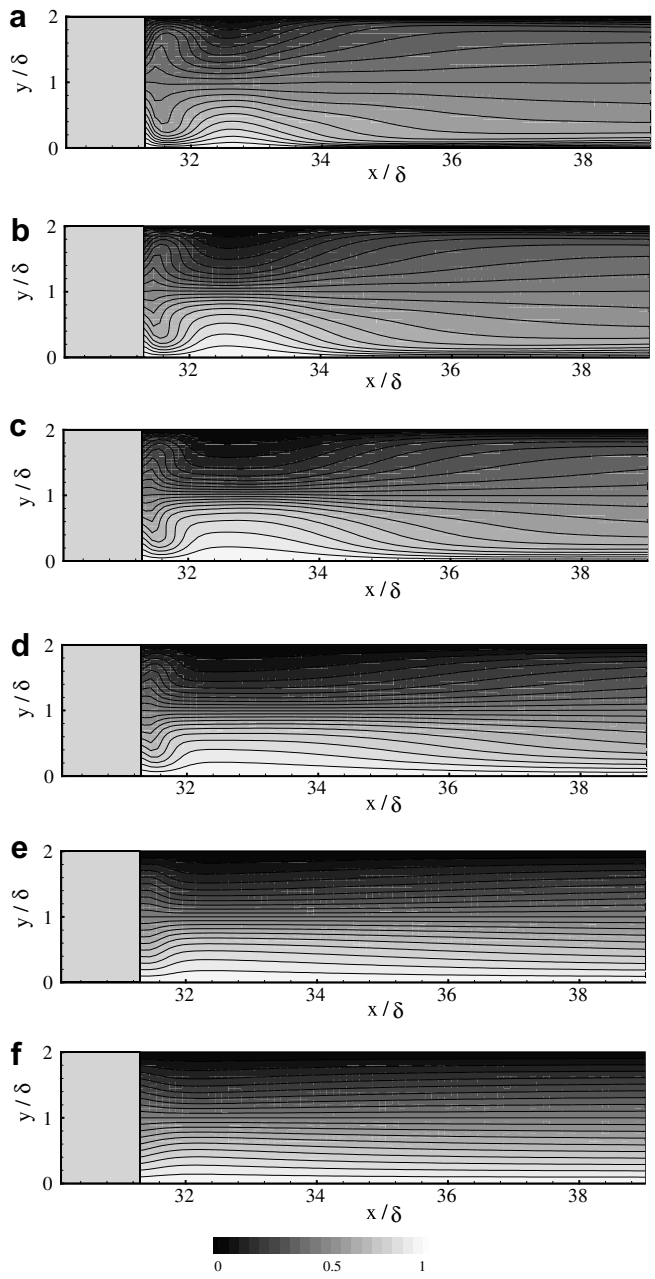

Fig. 13. Contours of the time-averaged temperature in the downstream region of the prism in the x–y plane of symmetry; (a) $Re_\tau = 80$; (b) $Re_\tau = 60$; (c) $Re_\tau = 50$; (d) $Re_\tau = 40$; (e) $Re_\tau = 30$; (f) $Re_\tau = 20$.

much smaller than that of the turbulence transport. The heat transfer enhancement by the convection is indeed dominant around the prism. This effect is confined to the vicinity of the prism. Hence, the mean flow itself does not directly augment the spatial-averaged Nusselt number $\langle\overline{Nu}\rangle$. Accordingly, we can conclude that the three-dimensional mean flow around the prism produces the turbulence and thus the dispersion of the induced turbulence contributes most significantly to the holistic heat transfer augmentation.

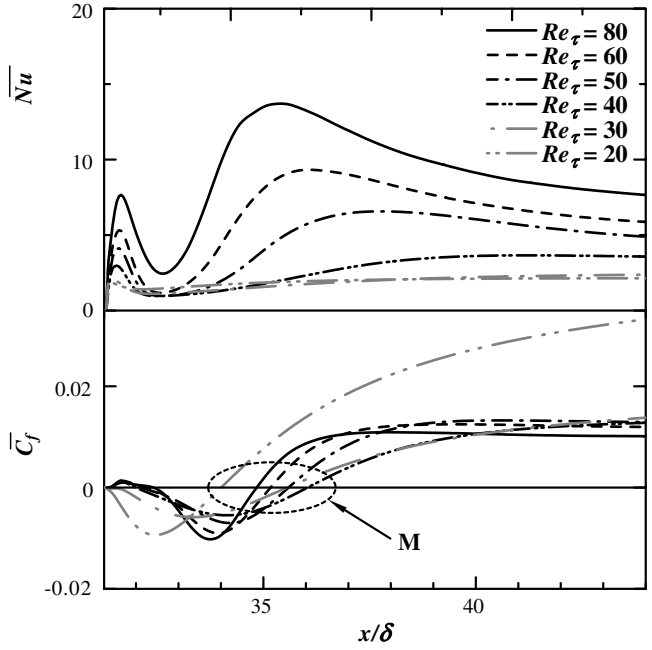

Fig. 14. $\overline{C_f}$ and $\overline{Nu}$ in the downstream region of the prism in the symmetry plane on the bottom wall.

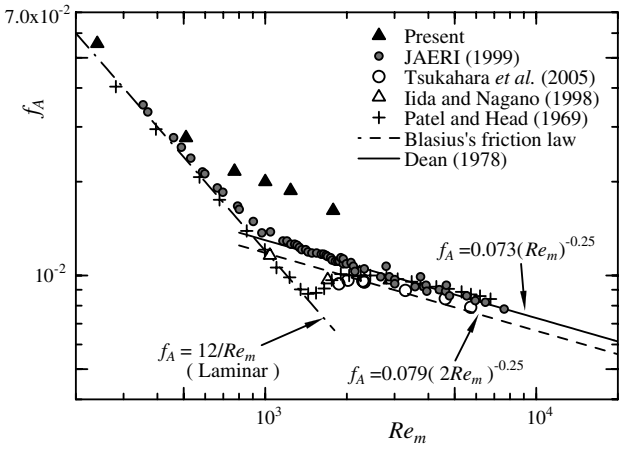

Fig. 15. Variation of friction factor f_A with Re_m.

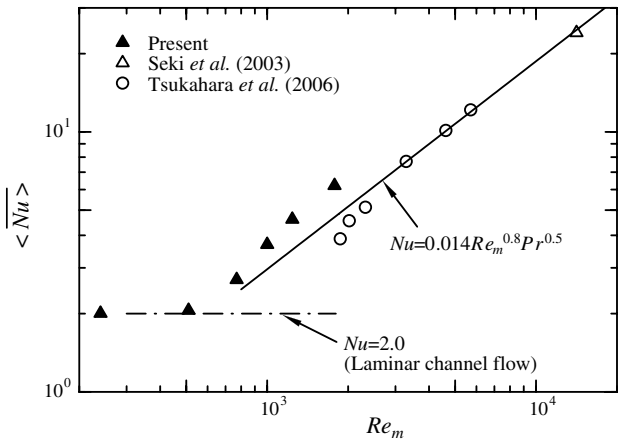

Fig. 16. Variation of the time- and spatial-averaged Nusselt number $\langle\overline{Nu}\rangle$ with Re_m.

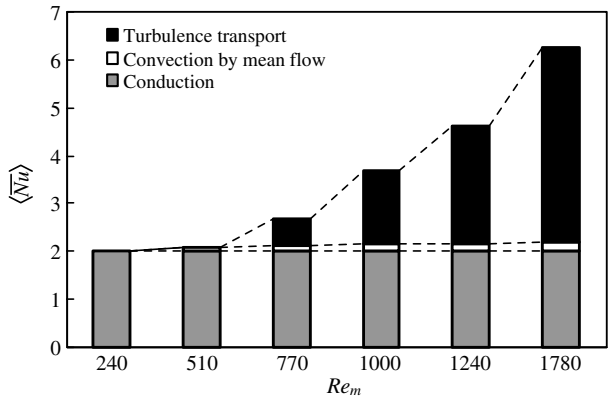

Fig. 17. Contribution of the conduction, the mean flow convection and the turbulence transport to $\langle\overline{Nu}\rangle$.

4. Conclusions

DNS of heat transfer in a channel flow obstructed by rectangular prisms has been performed for low Reynolds numbers in order to assess the effect of the prism on the flow and the heat transfer in the turbulent-laminar transition range. The Reynolds number effect on the time-averaged vortex structure around the prism is discussed. The relation between the vortex structure and local heat transfer is also investigated. In addition, the effect of the prism on the mean flow parameters is presented.

In the instantaneous flow field, the near-wall streaky structures are observed in the whole calculated domain for $Re_\tau = 80$, 60 and 50. For $Re_\tau = 40$, the number of the streaky structures decreases except in the near wake region in comparison with the cases of higher Re_τ. Moreover, the flow results in steady laminar flow for $Re_\tau = 30$ and 20.

In the time-averaged flow field, the complex vortices wrap around the prism. Upstream of the prism, the horseshoe vortices are generated. The size of them is almost unchanged for all the calculated cases for $Re_\tau = 80$–30. In this region, the heat transfer is remarkably enhanced because of the low temperature-fluid impingement induced by the prism and the washout effect of the horseshoe vortices. The width of the area with remarkably enhanced heat transfer is approximately δ from the front-end prism for all the cases.

Around the lateral region of the prism, four longitudinal vortices are formed. The size of these vortices are almost unchanged for $Re_\tau = 80$–50. For $Re_\tau = 40$–30, these vortices become weak with decreasing Reynolds number. For $Re_\tau = 20$, these vortices are not clearly observed. In this region, the heat transfer is significantly enhanced because of the same mechanism in the upstream region.

Downstream of the prism, the flow pattern strongly depends on Reynolds number. The meeting line first shifts towards the downstream direction with decreasing Reynolds number for $Re_\tau = 80$–40, and approaches to the back-end prism for $Re_\tau = 30$ and 20. Downstream of these meeting line, a relatively large local peak of $\overline{Nu}$ was observed for $Re_\tau = 80$–40. This local peak arises from the enhanced mixing around the meeting line. However, no significant correlation can be found between the meeting point and the local peak.

The turbulence budgets also provide understandings to the interaction of vortices downstream of the obstacle and its influence on heat transfer. The rest of the data, such as the turbulence budgets, will be uploaded on our web of DNS database"http://murasun.me.noda.tus.ac.jp/turbulence/".

The friction factor does not show the drop in the turbulent-laminar transition range. This is because the turbulence remains owing to the disturbance produced around the separation and the wake region of the prism. The values of $\langle\overline{Nu}\rangle$ stay larger than the empirical correlation of the turbulent plane channel flow even in the transition range. The contributions of the conduction, the mean flow convection and the turbulence transport to $\langle\overline{Nu}\rangle$ are examined. It is statistically confirmed that the dispersion of the turbulence induced by the prism contributes most significantly to the holistic heat transfer augmentation.

Acknowledgements

The present computations were performed with the use of supercomputing resources at Information Synergy Center of Tohoku University, and also VPP5000/64 at Computing and Communications Center of Kyushu University.

References

Dean, R.B., 1978. Reynolds number dependence of skin friction and other bulk flow variables in two-dimensional rectangular duct flow. ASME J. Fluid Eng. 100, 215–222.

Dukowicz, J.K., Dvinsky, A.S., 1992. Approximate factorization as a high order splitting for the implicit incompressible flow equations. J. Comp. Phys. 102, 336–347.

Fadlun, E.A., Verzicco, R., Orlandi, P., Mohd-Yousof, J., 2000. Combined immersed-boundary finite-difference methods for three-dimensional complex flow simulations. J. Comp. Phys. 161, 35–60.

Fukagata, K., Iwamoto, K., Kasagi, N., 2005. Novel turbulence control strategy for simultaneously achieving friction drag eduction and heat transfer augmentation. In: Proceedings of 4th International Symposium Turbulence and Shear Flow Phenomena, pp. 307–312.

Hussein, H.J., Martinuzzi, R.J., 1996. Energy balance for turbulent flow around a surface mounted cube placed in a channel. Phys. Fluids 8 (3), 764–780.

Hwang, J.Y., Yang, K.S., 2004. Numerical study of vortical structures around a wall-mounted cubic obstacle in channel flow. Phys. Fluids 16 (7), 2382–2394.

Iida, O., Nagano, Y., 1998. The relaminarization mechanisms of turbulent channel flow at low Reynolds numbers. Flow, Turbul. Combust. 60, 193–213.

Japan Atomic Energy Research Institute, 1999. Thermal and fluid-dynamic research and development for high temperature gas cooled reactor In: K. Sanokawa (Ed.), vol. 88. JAERI. JAERI-Review, pp. 98–024 (in Japanese).

Larousse, A., Martinuzzi, R., Tropea, C., 1991. Flow around surface-mounted, three-dimensional obstacles. In: Proceedings of the Eighth Symposium on Turbulent Shear Flows, vol. 1. pp. 14-4-1–14-4-6.

Martinuzzi, R., Tropea, C., 1993. The flow around surface-mounted, prismatic obstacles placed in a fully developed channel flow. ASME J. Fluids Eng. 115, 85–92.

Meinders, E.R., Hanjalić, K., 1999. Vortex structure and heat transfer in turbulent flow over a wall-mounted matrix of cubes. Int. J. Heat Fluid Flow 20, 255–267.

Meinders, E.R., Hanjalić, K., Martinuzzi, R.J., 1999. Experimental study of the local convection heat transfer from a wall-mounted cube in turbulent channel flow. ASME J. Heat Transfer 121, 564–573.

Morinishi, Y., Lund, T.S., Vasilyev, O.V., Moin, P., 1998. Fully conservative higher order finite difference schemes for incompressible flow. J. Comp. Phys. 143, 90–124.

Patel, V.C., Head, M.R., 1969. Some observations on skin friction and velocity profiles in fully developed pipe and channel flows. J. Fluid Mech. 38, 181–201.

Robinson, S.K., 1991. Coherent motions in the turbulent boundary layer. Annu. Rev. Fluid Mech. 23, 601–639.

Seki, Y., Abe, H., Kawamura, H., 2003. DNS of turbulent heat transfer in a channel flow with different thermal boundary conditions. In: Proceedings of 6th ASME/JSME Thermal Engineering Conference, 248.

Seki, Y., Iwamoto, K., Kawamura, H., 2006. Prandtl number effect on turbulence quantities through high spatial resolution DNS of turbulent heat transfer in a channel flow. In: Proceedings of 5th International Symposium on Turbulence, Heat and Mass Transfer, pp. 301–304.

Tsukahara, T., Seki, Y., Kawamura, H., Tochio, D., 2005. DNS of turbulent channel flow at very low Reynolds numbers. In: Proceedings of International Symposium TSFP4, pp. 935–940.

Tsukahara, T., Iwamoto, K., Kawamura, H., Takeda, T., 2006. DNS of heat transfer in a transitional channel flow accompanied by a turbulent puff-like structure. In: Proceedings of 5th International Symposium on Turbulence, Heat and Mass Transfer, pp. 193–196.

Yakhot, A., Liu, H., Nikitin, N., 2006. Turbulent flow around a wall-mounted cube: a direct numerical simulation. Int. J. Heat Fluid Flow 27, 994–1009.